CrystEngComm

PAPER

View Article Online
View Journal | View Issue

Published on 22 June 2016. Downloaded by Synchrotron Radiation Library on 11/09/2017 10:06:28.

Cite this: *CrystEngComm*, 2016, **18**, 5860

Self-aligned synthesis of a NiPt-alloy$_{core}$@Pt$_{shell}$ nanocrystal with contrivable heterojunction structure and oxygen reduction activity†

Tsan-Yao Chen,‡*[ab] Sun-Tang Chang,[c] Chih Wei Hu,[a] Yen-Fa Liao,[c] Ying Jhen Sue,[d] Yang-Yang Hsu,[a] Kaun-Wen Wang[e] and Yu-Ting Liu‡*[d]

Received 21st May 2016,
Accepted 22nd June 2016

DOI: 10.1039/c6ce01182a

www.rsc.org/crystengcomm

A bimetallic NiPt nanocrystal (NC) has been synthesized using the wet chemical reduction method; it was sequentially designed in the presence of carbon nanotubes. NiPt@Pt NC is a nanocrystal with the configuration of a NiPt alloy core and tuneably thick Pt shell. Under optimum conditions (Pt = 20 at%), the oxygen reduction current of NiPt@Pt NC is 1.08-fold at 0.85 V (*vs.* RHE), as compared to Pt NC, and the onset voltage (V_{OC}) is 0.905 V. The results of the atomic and crystal structure analyses show that such an enhancement is largely due to the impact of the local strain and the electronic dipole at the heterogeneous Pt–Ni interface. Most importantly, we have proposed a robust technique for programming the atomic structural configuration and oxygen reduction activity of NC, which shows comparable performance and ~80% less Pt loading than Pt NC.

Introduction

The development of nanocatalysts (NC) in fuel cell techniques involves three long-standing issues: material cost, reactivity, and electrochemical reliability. Most discussions on these issues are geared towards the composition and configuration of the employed NC components. Among the existing configurations, NC, with a core–shell structure, proper surface decoration, and shell crystal thickness is recognized as an ideal design, in terms of the reactivity and durability of the NC in energy conversion devices (*e.g.*, fuel cells, dye-sensitized solar cells, water splitting cells, and CO_2 converters).[1] The altered configuration has to go through a series of redox reaction steps, including homogeneous nucleation, crystal growth, and allocation of shell atoms on selected core crystallites.

For the redox selectivity, reactivity, and durability of anodic and cathodic NC in fuel cells, one direct approach is to manipulate the strain vector in the shell crystal region by properly allocating the selected core–shell components.[2] In contrast to the traditional designs, NC with core–shell structures largely improve the lifetime of the fuel cell system; in particular, the work cycle increases (>0.1–1.0 M) and the device efficiency is better (55–65%).[1b,2d,3] The effects of the near surface lattice strain are significant to the electrochemical properties of anodic and cathodic NC. These substantial improvements are further confirmed by the intra-particle heterojunction, where a strong electronegative shell crystal or one with high lattice energy is grown on top of transition metals or metal oxides.[1b] With calculations in density functional theory (DFT) and experimental characterizations, one can notice that the physiochemical properties of core–shell NP are optimized by minimizing the shell crystal thickness and maximizing the interfacial electron dipole coupling effects.[4]

The over potential and activity of NC at the cathodic reaction (oxygen reduction reaction, ORR) are key indexes for developing a high power fuel cell system.[2c,5] In a direct methanol fuel cell (where Pt is employed at the cathode), it is particularly important for NC to undergo suppressed methanol oxidation activity and comparable ORR activity to Pt. In pursuing the ideal catalysts, a growing body of research has been devoted to the optimization of chemical composition, structure configuration, and supporting materials of NC.[6] Previous spectroscopy techniques have proved the heteroatomic hybridization of transition metal dopants in terms of the durability and activity of NC in different steric configurations.[7] In this work, a robust wet chemical method is

[a] *Department of Engineering and System Science, National Tsing Hua University, Hsinchu 30013, Taiwan. E-mail: chencaeser@gmail.com; Tel: +886 3 5715131#34271*
[b] *Institute of Nuclear Engineering and Science, National Tsing Hua University, Hsinchu 30013, Taiwan*
[c] *National Synchrotron Radiation Research Center, Hsinchu 30076, Taiwan*
[d] *Department of Soil and Environmental Science, National Chung Hsing University, Taichung 402, Taiwan. E-mail: yliu@nchu.edu.tw*
[e] *Institute of Materials Science and Engineering, National Central University, Taiwan*

† Electronic supplementary information (ESI) available: The cyclic vlotametry sweeping curves for determining the electrochemical surface area of experimental NCs were enclosed. See DOI: 10.1039/c6ce01182a

‡ T.-Y. Chen and Y.-T. Liu are co-correspondence to this paper.

This journal is © The Royal Society of Chemistry 2016

Published on 22 June 2016. Downloaded by Synchrotron Radiation Library on 11/09/2017 10:06:28.

developed, with sequence and reaction time control in synthesizing the NiPt@Pt (NiPt alloy in the core, underneath a Pt enriched shell crystal) NC, which shows the tuneable shell thickness and ORR activity. We demonstrate that the atomic arrangement is determined by lattice relaxation when the amount of Pt atoms are changed in the shell crystal. Under optimum conditions, the current density of the NiPt@Pt is enhanced by ~8% at 0.85 V (*vs.* RHE) with a higher onset voltage (V_{OC} = 0.905 V *vs.* RHE) than that of Pt NC. Details of the heteroatomic intermixing in relation to the electrochemical performance of NC are given in the following sections.

Experiment

Synthesis of NiPt@Pt NC

The NiPt@Pt as a NC comprised of a NiPt alloy core and Pt rich shell crystal was synthesized using the wet chemical reduction method, with sequence and reaction time control. In the first step, 50.0 mg of carbon nanotubes (CNT, Cnano Technology Ltd.) were immersed in a $NiCl_2{\cdot}6H_2O_{(aq)}$ (99%, Sigma-Aldrich Co.) solution and stirred at 250 rpm at 25 °C for 12 h. This solution (solution A) contained 61.5 mg $NiCl_2{\cdot}6H_2O$ (*i.e.*, 15.0 mg = 0.063 mmole of Ni metal ion) and 30 g distilled water. After immersion, 3.0 ml of aqueous solution containing 10.0 mg (0.252 mmole) $NaBH_{4(aq)}$ (99%, Sigma-Aldrich Co.) was dropped into solution A and stirred at 250 rpm for 15 s. Then, the Pt precursor solution containing 1.0 ml distilled water and 39.7, 105.9, and 172.1 mg (*i.e.*, 0.025–0.082 mmoles) of $H_2PtCl_6{\cdot}6H_2O$ (99%, Sigma-Aldrich Co.) was dropped into the solution mixture for preparing the NC with the Pt/Ni atomic ratios of 0.3, 0.8, and 1.3. In this step, a restructuring between Pt and Ni atoms arises from a simultaneous galvanic replacement of Ni with Pt^{4+}, followed by the reduction of residual metal ions with H: radicals. Details of the reaction pathways are given in the ESI.† For ease of understanding, the NiPt@Pt samples are named Ni@Pt20, Ni@Pt40, and Ni@Pt56, according to the Pt content of NC.

Preparation of the slurry sample and the method for the ORR experiment

The slurry sample for the ORR experiment was made of 5.0 mg CNT supported NiPt@Pt NC, mixed with distilled water (14.0 ml), IPA (6.0 ml), and 5 wt% Nafion (0.1 ml). The mixture was stirred at 250 rpm for 30 min before the 30 min ultrasonication treatment at 30 °C. For preparing the working electrode in the ORR sweeping experiment, the slurry (20.0 μl) was dropped and dried on top of a rotating graphite electrode (diameter = 5.0 mm). The linear sweep voltammetry (LSV) data were collected using a potentiostat (CH Instruments Model 600B) equipped with a three-electrode electrochemical system. This system consists of a standard electrode of Ag/AgCl (the voltage was calibrated by 0.203 V, in alignment with that of RHE), a counter electrode of Pt metal wire, and a working electrode. The electrolyte was an aqueous solution of $HClO_4$ (0.5 M) and the voltage scan rate was 0.5 mV s^{-1}.

NC characterization

The crystal structure of NC was characterized by high resolution transmission electron microscopy (HRTEM) at the Center for Electron Microscopy at National Sun Yat-sen University of Taiwan. The atomic structural parameters of NC were determined by X-ray absorption spectroscopy (XAS) and the spectra were measured at beamlines BL-07A, BL-17C at the National Synchrotron Radiation Research Center (Hsinchu, Taiwan), and BL-12B2 of Spring-8 (Japan). The NC nanostructures (particle size, size distribution, and shape) were determined by small-angle X-ray scattering (SAXS) analysis, where the scattering spectra were measured at beamline BL-23A at NSRRC in Taiwan. The chemical composition of NC was determined by X-ray photoemission spectroscopy (XPS) and the spectra were measured at beamline BL-24A at NSRRC in Taiwan.

Results and discussion

Crystal structure and nanostructure of NiPt@Pt NC

We used HRTEM to confirm the evolution of the crystal structures, particle shapes, and near surface atomic arrangements of NC, which are affected by different Pt/Ni ratios. As indicated in Fig. 1a, the Pt NC (diameter of ~4.5 nm) was grown in a hexagonal shape, which is the projection image of a cubic shape at the zone axis of the (111) facets (2.26 Å) coinciding at the centre. A slight shape distortion is due to the slant of the {111} zone axis with a small angle from the projection direction of the incident electron beam. The preferential growth of (111) and (200) facets (as proved by the two sets of symmetry point patterns in the Fourier transform (FT) image, inset) accounts for the surface energy minimization and the stabilization of carbonaceous ligands in high surface energy facets.[8] For core–shell NC, as indicated by white arrows in Fig. 1b and c, Ni@Pt20 and Ni@Pt40 are grown by stacking (111) facets in different directions of the multifaceted twin crystal.[8–9] The presence of clear twin boundaries (red arrows) suggests the formation of a semicoherent interface by lattice relaxation. In Ni@Pt20 (Fig. 1b), significant dislocations (distorted lattice fringes with position offset) are found at two sides of arrows A. This is a typical feature of the strong lattice strain at the heterogeneous interface. As a result, the lattice space of these fringes is 2.21 Å and is compressed by 2.6% from that of the ideal Pt(111) facet (2.26 Å). Given that the theoretical lattice mismatch between the Ni(111) (d = 2.03 Å) and Pt(111) (d = 2.26 Å) facets is 10.1%, the reduced lattice compression rationalizes the lattice relaxation by the formation of dislocations and the core alloy in NC. The preferential lattice mismatch is further elucidated by the corresponding Fourier transform (FT) image (Fig. 1 inset). As shown in Fig. 1b inset, two sets of FT lines (L1 and L2) of different lengths illustrate the formation of two misaligned lattice fringes in the core–shell interface of NC. The longer FT line

Published on 22 June 2016. Downloaded by Synchrotron Radiation Library on 11/09/2017 10:06:28.

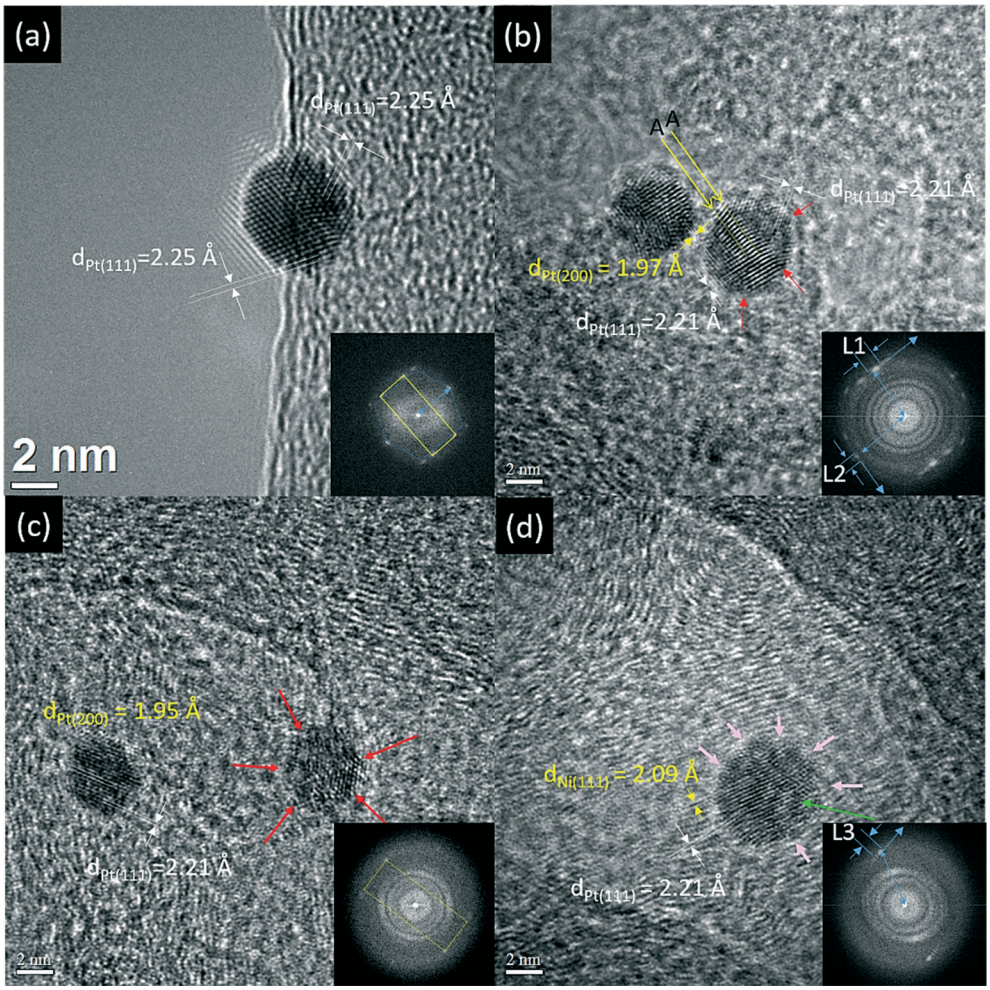

Fig. 1 HRTEM images of (a) Pt, (b) Ni@Pt20, (c) Ni@Pt40, and (d) Ni@Pt56 NCs; the insets demonstrate the corresponding Fourier transform (FT) images. In these FT images, the presence of two sets of FT lines suggests the formation of twin, or highly mismatched lattice fringes in two orientations. The longer L1 than L2 indicates the preferential lattice structure in Ni@Pt20.

in the short R ring (L1) denotes the preferential mismatch in the wide lattice space interface (*i.e.*, Ni(111)@Pt(111)), compared to Ni(111)@Pt(200), or Ni(200)@Pt(200). The lattice strain in NiPt@Pt is substantially reduced by increasing the Pt content. For Ni@Pt40 (Fig. 1c), NC is grown as hexagons and octagons along the latitudinal and longitudinal axes, resulting in an icosahedral crystal. Again, the formation of a twin crystal is confirmed by FT image (Fig. 1c inset), where the hexagonal pattern indicates the formation of a multifaceted (111) crystal in the shell region. Only one pattern is found in the FT image, suggesting that there is one form of lattice mismatch at the (111) facets in the core–shell interface. This characteristic accounts for the lattice relaxation of the Pt shell crystal *via* interface alloying with increasing shell crystal thickness, greater than 3 atomic layers.[10] Given that no stabilizer (*i.e.*, surfactant or polymers) is employed, the growth of the core–shell crystal in the anisotropic icosahedron can be explained by the uneven heterogeneous shell crystal growth rate between different facets. The heterogeneous crystal growth rate is determined by the difference in surface energy and atomic arrangements (symmetry) between crystal facets in the core (*i.e.*, substrate) and shell regions. The theoretical surface energy (E_γ) of Ni and Pt crystals at difference facets is summarized in Table S3.† Accordingly, E_γ is 2.011/2.299 (J m^{-2}) for (111), 2.426/2.734 (J m^{-2}) for (100), and 2.368/2.819 (J m^{-2}) for the (110) facets of the Ni/Pt metal crystal.[11] In a thermodynamically balanced reaction system, the nucleation and crystal growth of the system tend to minimize the surface energy. Therefore, it is understandable to find the preferential growth of Pt(111) facets on top of the high surface energy facets (*i.e.*, (100) and (110) facets) on the Ni core surface. In this case, a greater extent of heteroatomic intermixing between Pt and Ni atoms in the (100) and (110) facets, compared to the (111) facets of the Ni core is expectable. This result is attributed to the galvanic replacement between Pt^{4+} and Ni metal atoms in the core crystal surface and the reduction of surface free energy when capping Pt(111) facets at high E_γ facets of the Ni core ((100) and (110) facets). By increasing Pt to 56 at%, the lattice relaxation reaches the maximum extent among the current NCs. This characteristic is

 This journal is © The Royal Society of Chemistry 2016

Published on 22 June 2016. Downloaded by Synchrotron Radiation Library on 11/09/2017 10:06:28.

proved by the formation of sphere – like NC with a distinct core–shell interface (green arrow in Fig. 1d). As can be seen, the lattice spacing of the (111) facets for Pt and Ni crystals is arranged in the same direction, with a slight tilt angle (less than 5°). The highly disordered surface atomic arrangement is evidence for the growth of discrete Pt shell crystal domains (denoted by pink arrows) at various facets of the core crystal in different orientations. For room temperature reaction, the interatomic diffusion/relocation kinetics is indistinct, due to the lack of thermal energy and thus, results in a high density of atoms and kinks in the outermost layer of the NC.

The HRTEM images depict that NiPt@Pt is grown in the core–shell structure in a shape transformed from multifaceted cylinder to sphere-like by increasing the Pt content from 20 to 56 at%. Regardless of the specific geometrical differences, these configurations can be mimicked by the core–shell cylinder, with poly-dispersity in the core and shell regions in an X-ray scattering model. In model refinement, the structural parameters of NC to be obtained include the average particle diameter "D_{avg}", the distribution of diameter "η_D" and length "η_L" of particle, the thickness of the shell crystal at the face "T_F" and the radial "T_R" facet, the radius "R_C" and length "L_C" of the core crystal. The SAXS spectra [$I(q)$ *vs.* q] of current NCs are compared in Fig. 2a and the obtained structural parameters are summarized in Table 1.

According to X-ray scattering theory, the features of a SAXS spectrum originate from the interferences of incident X-ray photons that are scattered by the surface geometry of inter-particle clusters in $q < 0.07$ Å^{-1} (structure factor, $F(q)$, in region A) and intra-particle structures (form factor, $P(q)$, in region B) of the NC in $q > 0.07$ Å^{-1}. Consequently, the SAXS spectrum can be described by combining the contributions of the fractal aggregate and the core–shell cylindrical models for Ni@Pt NCs in eqn (1).[12]

$$I(q) = A^{F}S(q)^{F}P(q)^{F} + A^{CSCPr}S(q)^{CSCPr}P(q)^{CSCPr} \quad (1)$$

where A is the number density of the scattering objects (*e.g.*, NC). Both $S(q)$ and $P(q)$ are functions of the momentum transfer (q) between incident and scattered X-rays. The superscripts F (fractal) and CSCPr (poly-dispersed core–shell cylinder) refer to which model the parameters belong.

There are four features, including (i) the slope in the scattering profile near the beam centre (S, which correlates to the size and stacking form of the scattering matter), (ii) the centre position (denoted by arrow X2) with (iii) width (W_X), and (iv) height (H_X) of the scattering hump in the high q region in a SAXS spectrum. The scattering profile in the near q zero region originates from the scattered X-rays at low incident contact angles. Hence, the value of S1 is contributed by the size of the scattering substances (*i.e.*, the size of the fractal aggregates for NC) and the intra-particle surface defects of the experimental NC.

A scattering hump (denoted by arrow X1) at q = 0.03–0.04 Å^{-1} is the contribution of the inter-particle correlation interference. Above 0.07 Å^{-1}, the X-ray scattering intensity rapidly

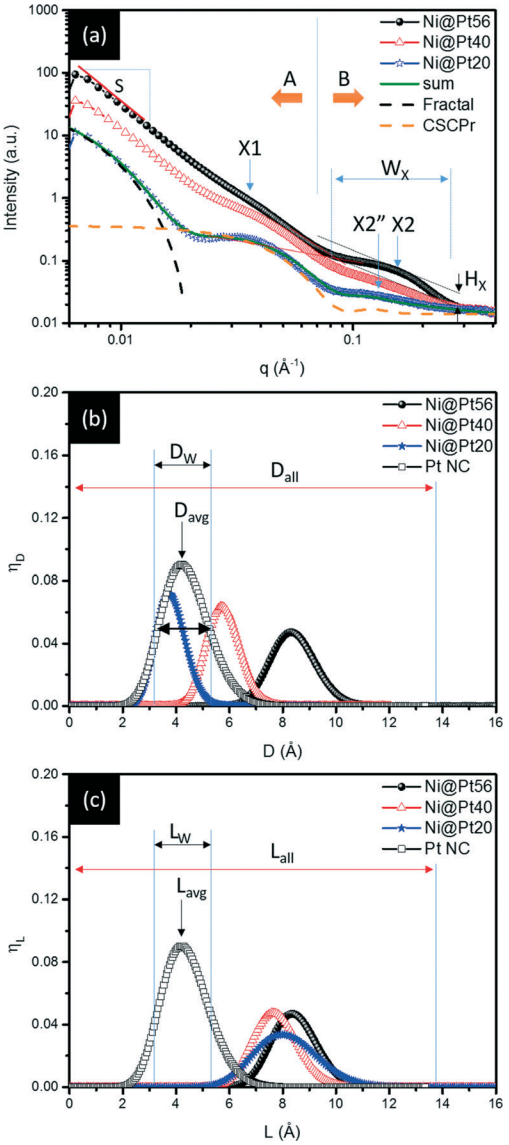

Fig. 2 (a) The small angle X-ray scattering spectra of NiPt@Pt and Pt NC. (b) and (c) Demonstrate the corresponding polydispersity of NC in diameter and length, respectively.

decreases with increasing momentum transfer (q). This phenomenon depicts the presence of out of phase scattering waves between the centre of the incident beam and the second order scattering maximum (denoted by arrow X2) in a SAXS spectrum, where q_X is inversely proportional to the size (or the aspect ratio of the longitudinal and latitudinal axes) and the shell crystal thickness (T_{shell}) of the NC. The scattering hump at X2 is the convolution interference of the X-ray waveforms at the intra-particle structures (*i.e.*, scattering within the core crystal region and between the core–shell interface and the outmost surface of the NC). Here, values of H_X and W_X are inversely proportional to the intra-particle interface roughness, the shell crystal thickness (T_F and T_R), and the dimensional parameters of the core crystal (*i.e.*, η_L, η_R, D_C). As indicated, the rising slope in the low q region suggests an increasing defect density in the NC surface with Pt/

Published on 22 June 2016. Downloaded by Synchrotron Radiation Library on 11/09/2017 10:06:28.

Table 1 SAXS determined structural parameters of NiPt@Pt NC

Sample	Pt (at%)	T_F[a] (nm)	T_R (nm)	L_C (nm)	D_C (nm)	D_{avg} (nm)	TSA (m^2 g^{-1})
Ni@Pt56	56	2.71	2.73	2.63	2.98		63.32
Ni@Pt40	44	1.98	2.96	4.13	1.82		69.82
Ni@Pt20	20	0.88	3.05	6.51	2.06		82.62
Pt NPs	100.00					4.15	47.41

[a] T_F (T_R), L_C (D_C), D_{avg}, and TSA denote the thickness of the shell crystal at the face (radial) facets, the average length (diameter) of the core crystal, the average diameter of Pt NP, and the theoretical surface area of NC, respectively.

Ni ratios. For Ni@Pt56, the indistinct X1 hump refers to a strong diffusion scattering intensity, as a result of the high roughness (defect density) in the NC surface. The inter-particle interference is progressively increased, which elucidates the reduced surface roughness and increased inter-particle packing density by decreasing the Pt content to 20 at%. In this event, the progressive suppression of the scattering intensity in the high q hump is with regard to the decreasing shell crystal thickness (2.91–1.68 nm for T_F and 2.71–0.88 nm for T_R), and the upshift of the 2nd scattering hump (X2″ → X2) with shell crystal growth depicting the reduction of the core crystal dimension (L_C from 6.51 to 2.62 nm). Considering the amount of the Pt precursor employed, the reduction of the core crystal size seems controversial; however, it is understandable on the basis of the protonation corrosion of metallic Ni atoms with galvanic replacement between Pt^{4+} and Ni metal, followed by the simultaneous reduction of Pt^{4+} and Ni^{2+} by H: radicals in the core crystal surface. These reactions result in the PtNi alloy core and $Pt_{1-x}Ni_x$ ($x \ll 1$) shell crystal (also proved by HRTEM in Fig. 1 and XAS analysis in Fig. 3). The distribution of diameter "η_D" and length "η_L" illustrate the changes in shell thickness at the radial and face facets. As depicted in Fig. 2b, D_{avg} of the Pt NC is 4.15 nm and η_D (W/D_{all}) is 13.5%. For NiPt@Pt NC, η_D increased by 4.6% (10.1–14.7%) when the Pt content was reduced from 56 to 20 at%. This is a consequence of the incomplete shell coverage, with a strong lattice match in the top of the core crystal in the radial face. In addition, D_{avg} of NiPt@Pt increased from 3.82 to 8.41 nm with Pt increasing to 56 at%. On the other hand, L_{avg} of NiPt@Pt is 8.16 ± 0.3 nm, without being affected by the Pt content. Combining the results for the structure evolutions of the core crystal, the growth rate of the shell

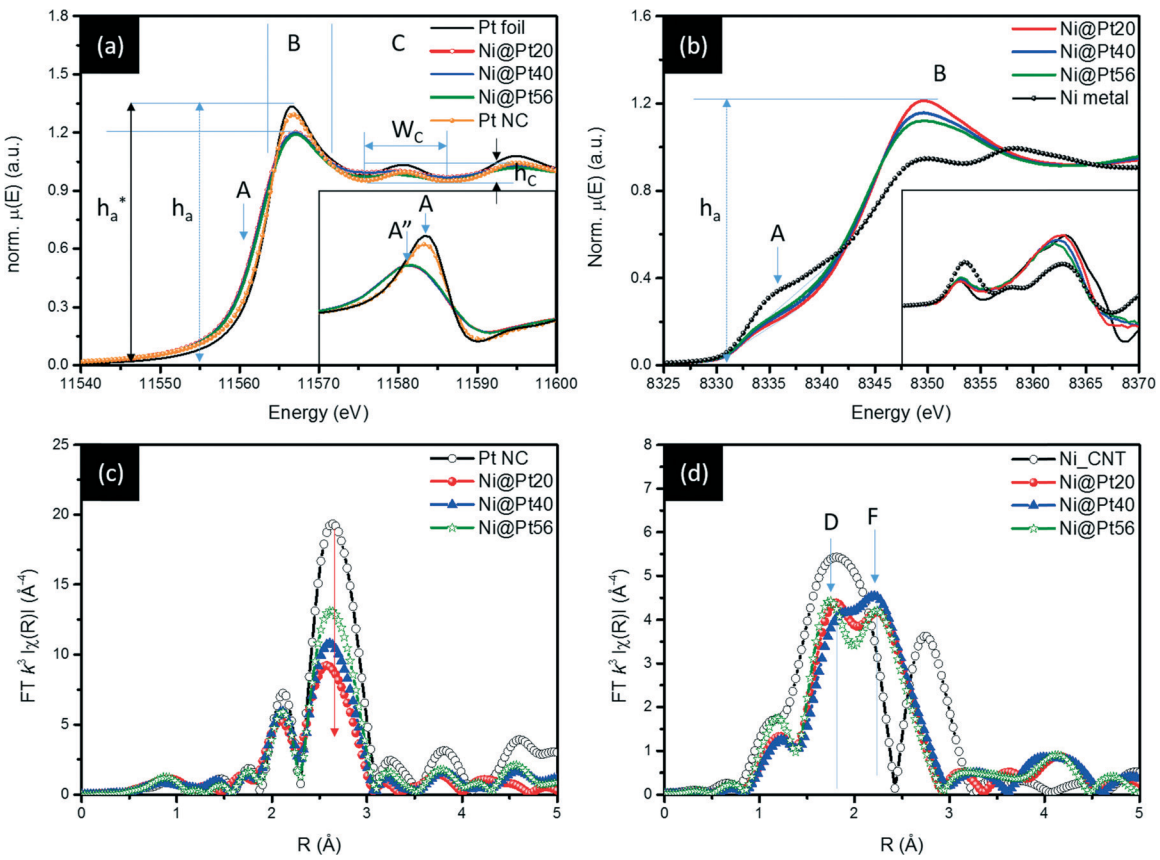

Fig. 3 The X-ray absorption near-edge spectra for experimental NC at (a) Pt L_3- and (b) Ni K-edges (insets show the first deviation curves). (c) and (d) Demonstrate the corresponding extended X-ray absorption fine structure spectra.

 This journal is © The Royal Society of Chemistry 2016

Published on 22 June 2016. Downloaded by Synchrotron Radiation Library on 11/09/2017 10:06:28.

crystal at the radial facets is significantly higher than that of the face facets on the Ni core surface. The uneven crystal growth explains a facilitation of heterogeneous nucleation – growth with a strong confinement on the shell crystal growth at selected facets. This confinement is commonly shown in the nucleation–growth of crystals with varied threshold (the interfacial mismatch and surface energy) of anion reduction in the heterogeneous interface of the NC exposed to the liquid phase. A possible pathway for facilitating the shell crystal growth is the severe protonation corrosion of atoms in the open core facets (*i.e.*, high Miller index facets). It creates the nucleation sites and reduces the barrier for allocation, followed by co-deposition of Pt and Ni atoms at radial facets by interacting with H: radicals in the NC surface.

Local atomic structure of NiPt@Pt NC

XAS analysis provides direct evidence for the formation of the PtNi alloy in the core region, and lattice relaxation in the shell region, by increasing the Pt content of NiPt@Pt. Fig. 3a (XANES spectra at the Pt L_3-edge) depicts the chemical states and the local atomic ordering of Pt atoms in the NC under inspection. In a L_3-edge spectrum, the position of inflection point (denoted by arrow A) denotes the threshold energy (E_0) for electron transitions from 2p to 5d orbitals, which is proportional to the oxidation state of transition metals. The white line intensity (h_a) and the width of the near-edge absorption peak (peak B) correspond to the extent of empty states and splitting of $5d_{5/2}$ orbitals. The width (W_C) and intensity (h_C) of peak C in the post-edge region illustrate the extent of local atomic ordering. Accordingly, the metallic characteristics of Pt atoms in Pt NC are evident, as revealed by the similar h_a intensity and inflection position (arrow A in inset) to that of Pt foil, where a slightly reduced h_C denotes the presence of surface defects. For NiPt@Pt, the suppressed h_a^* and h_C elucidate the lowered $2p_{3/2}$ to $5d_{5/2}$ transition and disturbed backscattering intensity, compared to Pt NC. The former suggests the strong electron relocation from Ni to Pt atoms (as consistently demonstrated by the downshift of the inflection peak from A to A″ in the inset) and the latter regards the local disorder around the Pt atoms. These feature the formation of the thin Pt shell crystal with a slight extent of heteroatomic intermixing (also declared by EXAFS analysis in Fig. 3c) in NiPt@Pt NC. The impact of Pt intermixing on electronic relocation between Pt and Ni is elucidated by Ni K-edge XANES. As shown in Fig. 3b, the intensity of the pre-edge (peak A) and the white line (h_a) denote the extent of charge transfer from 1s to 3d and 1s to 4p orbitals. Compared to Ni metal, the substantial suppression of peak A intensity and enhancement of h_a are indicators of the local distortion around Ni sites and the charge relocation from Ni 4p to neighbouring atoms in Ni@Pt20 NC. The intensity of near-edge (h_a) is progressively increased (or decreased) suggesting the decreasing local structural distortion (as well as the charge relocation from Ni to Pt) by increasing the Pt ratio to 56 at%.

The quantitative atomic structural parameters around Pt and Ni atoms declare the extent of the heteroatomic intermixing and the nanostructural configuration of NiPt@Pt. Fig. 3c and d show the Fourier transform radial structure functions (RSF) of the NCs under investigation at Pt L_3 and Ni K-edges (without phase correction), and the corresponding structural parameters are summarized in Table 2. As can be seen in Fig. 3c, the position of the radial peak in RSF at the 1st coordination shell is 2.741 Å (*i.e.*, the distance of the metallic Pt–Pt bond), suggesting the growth of metallic Pt crystal in Ni@Pt56.

Compared to that of Pt NC, the interatomic Pt–Pt distance (R_{Pt-Pt}) is reduced by 1.57% (~0.043 Å), implying a strengthened lattice compression by decreasing Pt to 20 at%. According to the atomic model simulation, the average coordination number (CN) is 6.51 for Pt–Pt (CN_{Pt-Pt}) and 0.53 for Pt–Ni (CN_{Pt-Ni}) bond pairs around Pt atoms in Ni@Pt56. These results indicate a heteroatomic intermixing (χ^{Ni} = CN_{Pt-Ni}/CN_{total_Pt}, CN_{total_Pt} = CN_{Pt-Pt} + CN_{Pt-Ni}) of 7.5% for Ni atoms in the Pt crystal region. By decreasing the Pt ratio from 56 to 20 at%, CN_{Pt-Pt} (CN_{Pt-Ni}) is determined to be 4.31 (1.11), suggesting the increase of χ^{Ni} from 7.5 to 20.4%.

In the Ni K-edge RSF spectra (Fig. 3d), the radial peaks at 1.81 and 2.25 Å stem from the backscattering interference of X-rays at Ni–Ni and Ni–Pt bond pairs in the 1st nearest coordination shell. For NiPt@Pt, R_{Ni-Ni} and R_{Ni-Pt} are 2.385 and 2.419 ± 0.01 Å, respectively. Compared to that of metallic Ni (2.522 Å), these values are reduced by 0.103–0.137 Å, which confirms a strong local structure distortion and large extent of heteroatomic intermixing of Pt atoms in the Ni crystal region (χ^{Pt}) in the NC. As revealed by the distorted pre-edge profile in Fig. 3b, such a structural distortion accounted for the formation of local NiPt alloy in the core and interface regions. According to atomic model simulations, CN_{Ni-Ni} (CN_{Ni-Pt}) is 2.27 (5.05) for Ni@Pt56, 2.05 (4.22) for Ni@Pt40, and 2.15 (4.43) for Ni@Pt20, with regards to χ^{Pt} (CN_{Ni-Pt}/CN_{total_Ni}, CN_{total_Ni} = CN_{Ni-Ni} + CN_{Ni-Pt}) of ~68% for NC in different Pt/Ni ratios. Taking the Pt L_3-edge results together, the uneven correlation of χ^{Pt} and χ^{Ni} with respect to Pt/Ni ratios again clarified the proposed NiPt alloy core and Pt shell structure in NCs. This hypothetical structure reflects the geometric configuration by SAXS analysis, where 14–25% of Pt shell atoms are located at the core–shell interface (Table S1† and in Scheme 1). The obtained structural information depicts that the NiPt@Pt NC is grown in the core–shell structure comprised of an alloy core crystal with high aspect ratio, a diffused core–shell interface, and a shell crystal with anisotropic thickness at different orientations, by growing different amounts of Pt in the shell crystal. This anisotropic crystal growth is due to the strong lattice mismatch and the surface energy difference between crystal facets in Ni and Pt crystals at the core–shell interface. Such an anisotropic junction induces the electron donation from Ni to Pt crystal and thus facilitates the ORR activity.

Oxygen reduction activity of NiPt@Pt NC

Fig. 4 shows the linear sweep voltammetry (LSV) spectra of Pt NC and NiPt@Pt with different Pt/Ni ratios. In the system, the electrolyte is a O_2-saturated $HClO_4$ solution (0.5 M) and

Published on 22 June 2016. Downloaded by Synchrotron Radiation Library on 11/09/2017 10:06:28.

Table 2 The model fitting determined local structural parameters of experimental NCs at Pt L_3 and Ni K-edges

	Pt L_3-edge				Ni K-edge			
Sample	Bind path	R (Å)	CN	$\chi^{Ni a}$	Path	R (Å)	CN	χ^{Pt}
Pt NPs	Pt–Pt	2.758	9.72	0				
Ni@Pt56	Pt–Pt	2.741	6.51	7.5	Ni–Ni	2.371	2.27	68.7
	Pt–Ni	2.606	0.53		Ni–Pt	2.409	5.05	
Ni@Pt40	Pt–Pt	2.728	5.31	15.6	Ni–Ni	2.404	2.05	67.3
	Pt–Ni	2.606	0.98		Ni–Pt	2.429	4.22	
Ni@Pt20	Pt–Pt	2.715	4.31	20.5	Ni–Ni	2.395	2.15	67.3
	Pt–Ni	2.606	1.11		Ni–Pt	2.429	4.43	

[a] χ^{Ni} (χ^{Pt}) denote the extent of heteroatomic intermixing for Ni (Pt) atoms in the Pt (Ni) crystal region.

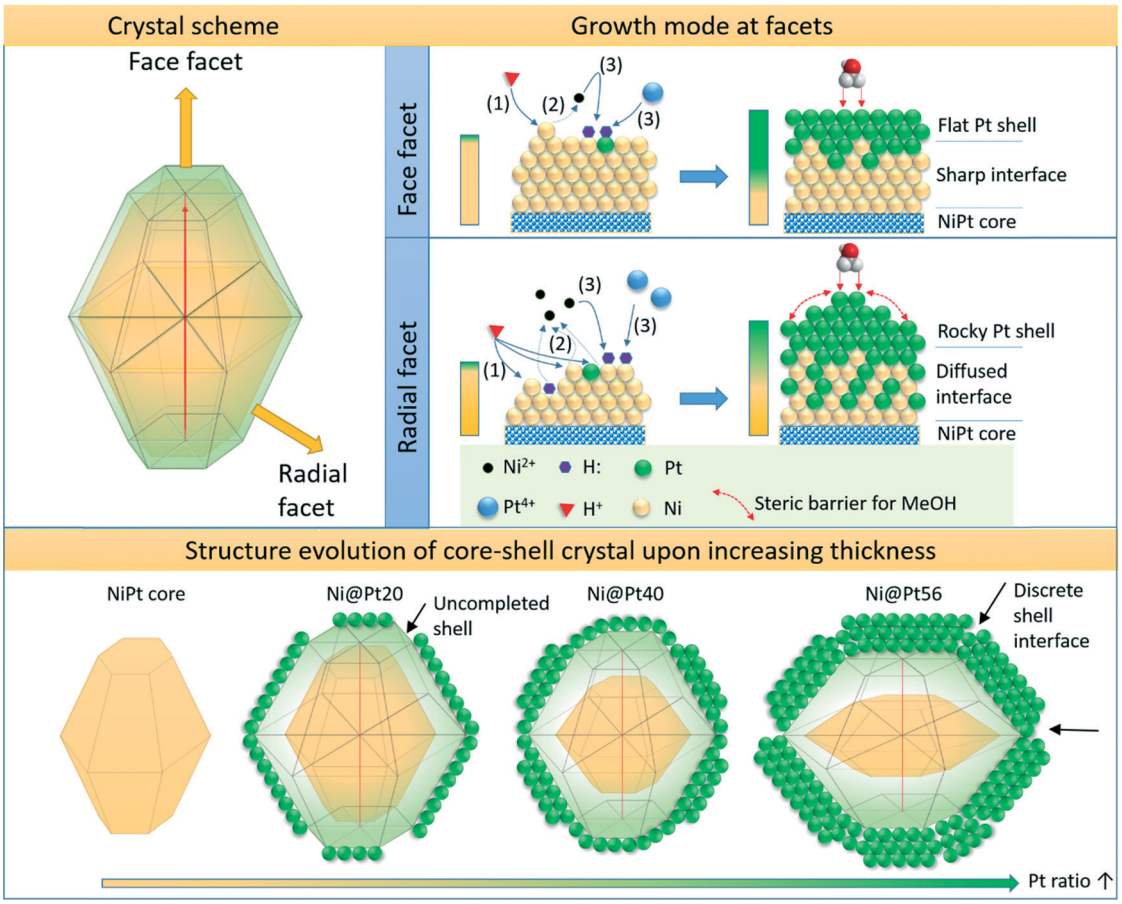

Scheme 1 The crystal scheme and corresponding shell crystal growth modes on the face and radial facets of the experimental NC. Three reaction pathways include (1) the protonation corrosion of the core surface atoms by H^+ ($H^+ + Ni^0 \rightarrow Ni^{2+} + H_2$; (2) diffusion of NI^{2+} and Pt^{4+} at the core surface; and (3) the reaction of N^{2+} and Pt^{4+} with H: radicals at the core surface. In these reactions, the rocky surface (radial facets) possesses severe protonation corrosion and therefore resulting in the diffused interface at the core–shell interface.

the rotation speed of the working electrode is 1600 rpm. As illustrated, the onset potential (V_{OC}) of NC under investigation follows the trend of Ni@Pt20 (a = 0.905 V) > Pt NC (b = 0.895 V) > Ni@Pt40 (c = 0.852 V) > Ni@Pt56 (d = 0.848 V), and is inversely proportional to their T_F (Table 1) and CN_{Pt-Pt} (Table 2). Moreover, their surface activity (SA, specific current densities *vs.* electrochemical surface area) also have the same sequence at 0.85 V. These characteristics suggest the promotion of ORR activity on NiPt@Pt by surface strain and local alloy. As shown in Fig. 4, SA (at 0.85 V) of NiPt@Pt increased from −0.35 to −1.26 mA cm^{-2}, by reducing the Pt content from 56 to 20 at%. In this event, NiPt@Pt truly demonstrates its merits in oxygen reduction with approximately 1.08-fold SA of Pt NC under optimum conditions. To clarify the effects of Pt content to surface electrochemical state and configuration of NC, the electrochemical analysis on multi-dentate, multi-nuclear chemisorption molecules (methanol in our case) was conducted. The corresponding results are

 This journal is © The Royal Society of Chemistry 2016

Published on 22 June 2016. Downloaded by Synchrotron Radiation Library on 11/09/2017 10:06:28.

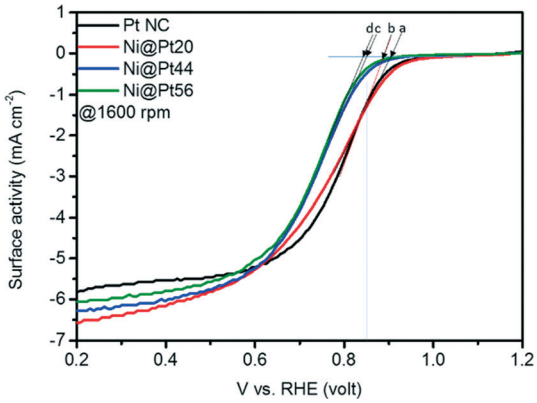

Fig. 4 The linear sweep voltammetry curves of experimental NC.

demonstrated in the ESI† (Fig. S1). Accordingly, the position of the methanol oxidation (MOR) peak is shifted by 1.1 V, accompanied by the current drop of ~70%, represented in the forward potential sweeping curve when the Pt content increased to 56 at%. These characteristics feature the increasing surface activation energy and the decreasing activation sites for the electrooxidation of methanol on the NiPt@Pt surface. Given that the electrochemical surface area for H^+ chemisorption is reduced by only 35% when increasing Pt to 56 at% (Table S1†), the dramatic MOR current difference reflects the formation of a discrete shell crystal, which contains a high density of surface defects (*i.e.*, kink/terrace defects of the steric barrier of the discrete shell interface in Scheme 1) and possibly the localized electronic dipoles at different core facets. These defects not only suppress the MOR and ORR activity, but also the electrochemical stability of NC (as illustrated by the current drop rate in long-term MOR testing of NC in Fig. S2†).

Conclusions

A robust method employing sodium borohydride as a reducing agent, with sequence and time controls, was developed for synthesizing the NiPt $alloy_{core}$–Pt_{shell} structured NC with contrivable shell thickness and surface configuration. We demonstrated that these NCs grow in multifaceted twin crystallites with an anisotropic growth rate across the latitudinal and longitudinal axes by changing the Pt content. Under optimum conditions (NiPt@Pt containing 20 at% of Pt), the ORR SA (at 0.85 V) was improved by 1.08 times and the V_{OC} was increased by 0.02 V, compared to Pt NC. Our structural characterizations elucidate that these enhancements are attributed to a lattice compression strain in the shell crystal, due to the unique structure of the NiPt alloy core underneath the Pt enriched shell crystal. Our XANES analysis disclosed that a prevailing heteroatomic intermix (bifunctional mechanism) and the strong electron donation from Ni to Pt sites (ligand and lattice strain effect) contribute to enhancing the ORR activity of NiPt@Pt. By increasing the Pt content to 56 at%, the preferential growth at the Pt(111)/Ni(111) interface results in the discrete shell crystal domains, therefore relaxing the lattice strain and reducing the number of reaction sites of NiPt@Pt. The electrochemical analysis proves that the surface reaction sites (ESCA) of NiPt@Pt are smaller than that of Pt NC. The evidence conclusively declares that the enhancement in ORR SA is accounted for by the electronic relocation by strain or ligand effects, instead of the particle size effect. Most importantly, a robust method with reduced synthesis time (<20 s) for growing the core–shell NC containing a low noble metal loading has been developed. This method provides a possible means for the low cost and rapid production of CNT supported cathodic NC for high current density fuel cell application.

Acknowledgements

The authors would like to thank the staff of National Synchrotron Radiation Research Center (NSRRC), Hsinchu, Taiwan for the help in various synchrotron-based measurements. The high resolution transmission electron microscopy (HRTEM) images were collected at center of electron microscopy, National Sun Yat-sen University, Taiwan. T.-Y. Chen acknowledges the funding support from research project of the Ministry of Science and Technology, Taiwan (MOST 103-2112-M-007-022-MY3). Y.-T. Liu acknowledges the funding support from research project of Ministry of Science and Technology, Taiwan (MOST 104-2311-B-005-016-MY3).

Notes and references

1 (*a*) B. J. Hwang, L. S. Sarma, J. M. Chen, C. H. Chen, S. C. Shih, G. R. Wang, D. G. Liu, J. F. Lee and M. T. Tang, *J. Am. Chem. Soc.*, 2005, **127**, 11140; (*b*) K. Sasaki, H. Naohara, Y. Cai, Y. M. Chio, P. Liu, M. B. Vukmirovic, J. X. Wang and R. R. Adzic, *Angew. Chem., Int. Ed.*, 2010, **49**, 8602; (*c*) Y. Ding, X. Sun, Z. L. Wang and S. Sun, *Appl. Phys. Lett.*, 2012, **100**, 111603.

2 (*a*) F.-J. Lai, W.-N. Su, L. S. Sarma, D.-G. Liu, C.-A. Hsieh, J.-F. Lee and B. J. Hwang, *Chem. – Eur. J.*, 2010, **16**, 4602; (*b*) S. Goto, S. Hosoi, R. Arai, S. Tanaka, M. Umeda, M. Yoshimoto and Y. Kudo, *J. Phys. Chem. C*, 2014, **118**, 2634–2640; (*c*) R. R. Adzic, J. Zhang, K. Sasaki, M. B. Vukmirovic, M. Shao, J. X. Wang, A. U. Nilekar, M. Mavrikakis, J. A. Valerio and F. Uribe, *Top. Catal.*, 2007, **46**, 249; (*d*) S. Alayoglu, A. U. Nilekar, M. Mavrikakis and B. Eichhorn, *Nat. Mater.*, 2008, **7**, 333.

3 P. Strasser, S. Koh, T. Anniyev, J. Greeley, K. More, C. Yu, Z. Liu, S. Kaya, D. Nordlund, H. Ogasawara, M. F. Toney and A. Nilsson, *Nat. Chem.*, 2010, **2**, 454.

4 T. Bligaard and J. K. Nørskov, *Electrochim. Acta*, 2007, **52**, 5512.

5 M. P. Hogarth and T. R. Ralph, *Platinum Met. Rev.*, 2002, **46**, 117.

6 (*a*) H. N. Nong, H.-S. Oh, T. Reier, E. Willinger, M.-G. Willinger, V. Petkov, D. Teschner and P. Strasser, *Angew. Chem., Int. Ed.*, 2015, **54**, 1; (*b*) E. L. Tae, J. Song, A. R. Lee, C. H. Kim, S. Yoon, I. C. Hwang, M. G. Kim and K. B. Yoon, *ACS Catal.*, 2015, 5525.

Published on 22 June 2016. Downloaded by Synchrotron Radiation Library on 11/09/2017 10:06:28.

7 (*a*) Y.-T. Liang, S.-P. Lin, C.-W. Liu, S.-R. Chung, T.-Y. Chen, J.-H. Wang and K.-W. Wang, *Chem. Commun.*, 2015, **51**, 6605; (*b*) H.-S. Chen, Y.-T. Liang, T.-Y. Chen, Y.-C. Tseng, C.-W. Liu, S.-R. Chung, C.-T. Hsieh, C.-E. Lee and K.-W. Wang, *Chem. Commun.*, 2014, **50**, 11165; (*c*) S.-P. Hsu, C.-W. Liu, H.-S. Chen, T.-Y. Chen, C.-M. Lai, C.-H. Lee, J.-F. Lee, T.-S. Chan, L.-D. Tsai and K.-W. Wang, *Electrochim. Acta*, 2013, **105**, 180; (*d*) S. M. Barnett, K. I. Goldberg and J. M. Mayer, *Nat. Chem.*, 2012, **4**, 498.

8 Y. Sun and Y. Xia, *Adv. Mater.*, 2002, **14**, 833.

9 S. Alayoglu and B. Eichhorn, *J. Am. Chem. Soc.*, 2008, **130**, 17479.

10 A. Schlapka, M. Lischka, A. Gross, U. Kasberger and P. Jakob, *Phys. Rev. Lett.*, 2003, **91**, 016101.

11 (*a*) J. Zhang, F. H. B. Lima, M. H. Shao, K. Sasaki, J. X. Wang, J. Hanson and R. R. Adzic, *J. Phys. Chem. B*, 2005, **109**, 22701; (*b*) A. Navrotsky, C. Ma, K. Lilova and N. Birkner, *Science*, 2010, **330**, 199; (*c*) P. J. Feibelman, *Phys. Rev. B: Condens. Matter*, 1995, **52**, 16845.

12 (*a*) J. Teixeira, *J. Appl. Crystallogr.*, 1988, **21**, 781; (*b*) A. Guinier and G. Fournet, *Small-Angle Scattering of X-Rays*, John Wiley and Sons, New York, 1955; (*c*) J. Wagner, *J. Appl. Crystallogr.*, 2004, **37**, 750.

 This journal is © The Royal Society of Chemistry 2016